Unconstrained Bezier Calibration Method for Nonlinear Measurement Calibration Applications: A Comparison Study

Hongliang Hua, Jingbo Zhao, Zhenqiang Liao, and Yongjiang Chen

The primary motivation of this paper is to present an accurate and universal method for the nonlinear system modeling. An Unconstrained Bezier Calibration Method (UBCM) is presented. By constraining the boundary freedom of the UBCM, it could become a constrained form called the Bezier Calibration Method (BCM), which is suitable for situations with an accurate boundary modeling requirement. A comparison study is performed to compare the presented method with the most widely utilized Polynomial Calibration Method (PCM) through several nonlinear behavior modeling examples, including sensor inherent nonlinearity calibration, sine wave, gauss nonlinearity and nonlinear broken line. A comparison study demonstrates that in the present verification examples the UBCM has better calibration performance than that of the BCM and PCM.

Calibration Modeling

It is well known that most sensors have an inherent nonlinearity which could affect their measurement accuracy and subsequently their control performance. Nonlinearity modeling and calibration are an essential requirement for a nonlinear measurement system [1], [2].

Nonlinear Modeling Method

Currently, several nonlinearity calibration methods have been developed, such as Polynomial Calibration Method (PCM) [3]–[5], neural network [6] and fuzzy logic calibration methods [7]. Among these methods, the PCM is the most widely utilized and has been applied in various fields such as sensor nonlinearity compensation [3], [8], [9], information fusion [10], and approximate modeling [11]–[15]. However, due to the Runge phenomenon of the PCM [16]–[18], there often exists a fluctuation error over the whole modeling range. The Runge phenomenon is quite common in the modeling of a system with strong nonlinearity, such as sinusoidal, Z type and other nonlinear types [19], [20]. A variety of work has been devoted to defeating the Runge phenomenon to improve the modeling accuracy of the PCM [21], [22] in nonlinear system applications. How to develop an accurate and universal calibration method for the nonlinear system modeling is still a challenging problem in the nonlinear measurement community [23], [24].

Research Motivation

The primary motivation of this paper is to present an accurate and universal calibration method for the nonlinear system modeling. An Unconstrained Bezier Calibration Method (UBCM) is presented, which is a more general form of our previously presented BCM model [20]. In the UBCM, a series of handle points and local weight coefficients are utilized to control the local modeling features. As a result, the UBCM could exhibit a strong nonlinearity modeling ability. A series of nonlinear models are utilized to quantitatively evaluate the calibration performance of the proposed UBCM and make a comparison with the previous BCM and PCM. The main contributions of this paper include:

- An Unconstrained Bezier Calibration Method (UBCM) is presented for nonlinear system modeling. The UBCM could achieve a nonlinear approximation of a set of discrete data globally, which has a broad application prospects such as sensor inherent nonlinearity calibration, system modeling and dynamic control [25].
- A sensor inherent nonlinearity calibration example is given to exhibit the effectiveness of the proposed UBCM in reducing measurement error and enhancing the measurement accuracy of a linear potentiometer.
- A comprehensive comparison of the UBCM, BCM and PCM is performed to provide a reference for engineering applications. In the comparison study, some typical nonlinear functions including sine wave, gauss nonlinearity and nonlinear broken line, are tested to evaluate the nonlinear modeling performance of the UBCM, BCM and PCM.

Calibration Method

In this case, we consider x and f as the calibrated data and reference value, respectively.

1094-6969/23/$25.00©2023IEEE

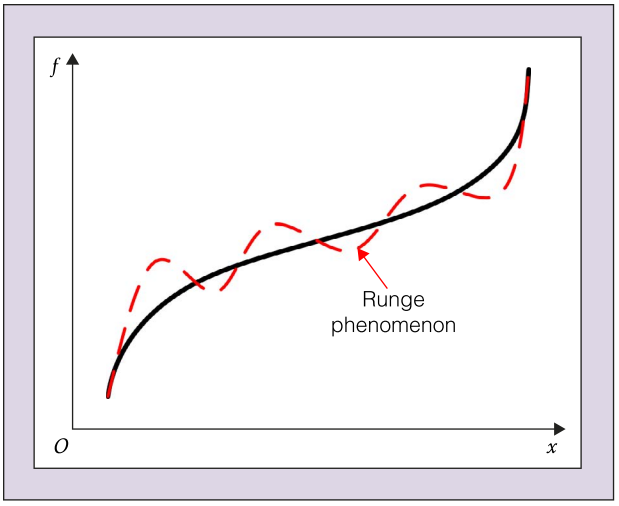

Fig. 1. Runge phenomenon of the PCM.

Polynomial Calibration Method (PCM)

According to [20], the polynomial calibration model is described as:

$$f_p(x)=\sum_{i=1}^{n+1}p_i x^{n-i+1} \tag{1}$$

where n and p_i denote the model order and unknown parameters. p_i could be obtained by minimizing e_{p2} as:

$$O_p=\min\left(\left\|e_p\right\|_2\right) \tag{2}$$

where $e_p=f\text{-}f_p(x)$ is the residual error of the PCM. Currently, PCM is the most commonly used method, since it has a concise form, as shown in (1). In dealing with strongly nonlinear modeling problems, the PCM needs to increase its model order n to achieve a better approximation. However, Runge phenomenon will occur in the higher-ordered polynomial calibration model. As depicted in Fig. 1, due to the increment of the model order, the polynomial calibration model fluctuates and deviates from target values. Therefore, in dealing with nonlinear problems, it is difficult for the PCM to obtain a good modeling accuracy even by increasing the model order. This is a significant drawback of the PCM.

Unconstrained Bezier Calibration Method (UBCM)

As depicted in Fig. 2a, take into consideration the measurement range into consideration, the unconstrained Bezier calibrating model could be established as:

$$f_{ub}(x)=\frac{\sum_{i=1}^{n+1}C_{n+1}^{i-1}w_{i-1}p_{i-1}\left(\frac{(x-l_x)}{r_x}\right)^{i-1}\left(1-\frac{(x-l_x)}{r_x}\right)^{n-i+1}}{\sum_{i=1}^{n+1}C_{n+1}^{i-1}w_{i-1}\left(\frac{(x-l_x)}{r_x}\right)^{i-1}\left(1-\frac{(x-l_x)}{r_x}\right)^{n-i+1}} \tag{3}$$

where n, p_i and w_i denote the model order and unknown parameters of the UBCM. l_x, u_x and $r_x=u_x\text{-}l_x$ denote the lower bound, upper bound and measurement range of x. Equation (3) could be rewritten as:

$$f_{ub}\left(\boldsymbol{p}_{ub},\boldsymbol{w}_{ub},x\right) \tag{4}$$

where $\boldsymbol{p}_{ub}=\left[p_1,\ldots p_n\right]^T$ and $\boldsymbol{w}_{ub}=\left[w_1,\ldots w_n\right]^T$ are unknown displacement and weight coefficient vectors.

Bezier Calibration Method (BCM)

As depicted in Fig. 2b, the UBCM is uncoordinated with the calibrated data at its boundary. Under some circumstances, sensor calibration may require an accurate approximation at the two bounds of the calibrated data x. To achieve an accurate calibration at the boundary of x, the unknown parameters of the 1st and n-th handle points could be constrained as $p_1=l_f$, $p_n=u_f$, $w_1=1$ and $w_n=1$, respectively. In this case, the UBCM becomes a constrained form, known as the Bezier Calibrating Method (BCM), as depicted in Fig. 2b. The BCM could be obtained as:

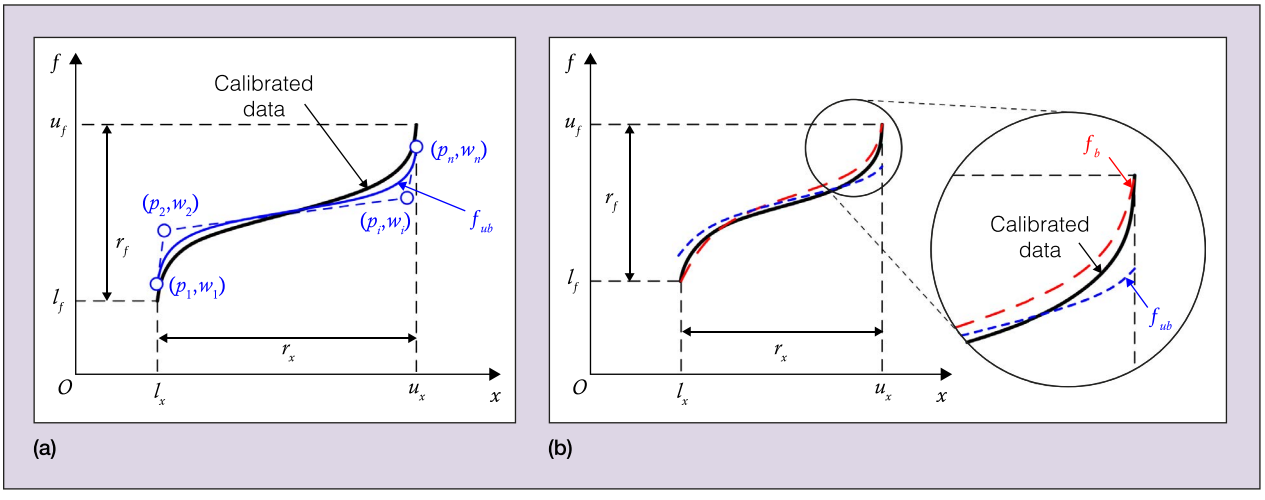

Fig. 2. (a) Illustration of the UBCM. (b) Illustration of the BCM.

$$f_b\left(\boldsymbol{p}_b, \boldsymbol{w}_b, x\right) \tag{5}$$

where $\boldsymbol{p}_b = \left[p_2, \ldots p_{n-1}\right]^T$ and $\boldsymbol{w}_b = \left[w_2, \ldots w_{n-1}\right]^T$ are unknown displacement and weight coefficient vectors. The main difference between (4) and (5) is are the dimensions of displacement and weight coefficient vectors. The unknown displacement and weight coefficient vectors $\boldsymbol{p}_{ub}$ and $\boldsymbol{w}_{ub}$, $\boldsymbol{p}_b$ and $\boldsymbol{w}_b$ of the UBCM and BCM, respectively, could be obtained by numerical optimization as:

$$\begin{cases} \boldsymbol{P}_{2n\times 1} = \begin{bmatrix} \boldsymbol{p}_{ub} \\ \boldsymbol{w}_{ub} \end{bmatrix} \in \left(\boldsymbol{l}_{ub}, \boldsymbol{u}_{ub}\right) \\ O_{ub} = min\left(\boldsymbol{e}_{ub2}\right) \end{cases} \tag{6}$$

$$\begin{cases} \boldsymbol{P}_{(2n-4)\times 1} = \begin{bmatrix} \boldsymbol{p}_b \\ \boldsymbol{w}_b \end{bmatrix} \in \left(\boldsymbol{l}_b, \boldsymbol{u}_b\right) \\ O_b = min\left(\boldsymbol{e}_{b2}\right) \end{cases} \tag{7}$$

where O_{ub} and O_b are objective functions of the UBCM and BCM optimization model, respectively. $(\boldsymbol{l}_{ub}, \boldsymbol{u}_{ub})$and $(\boldsymbol{l}_b, \boldsymbol{u}_b)$ denote the design space of design variables $\boldsymbol{P}_{2n\times 1}$ and $\boldsymbol{P}_{(2n-4)\times 1}$, respectively. $\boldsymbol{e}_{ub}$=$\boldsymbol{f}_{ub}$-$\boldsymbol{f}$ and $\boldsymbol{e}_b$=$\boldsymbol{f}_b$-$\boldsymbol{f}$ where $\boldsymbol{f}_{ub}$, $\boldsymbol{f}_b$ and $\boldsymbol{f}$ denote the discrete form of $f_{ub}(x)$, $f_b(x)$ and $\boldsymbol{f}$, respectively. The design space $(\boldsymbol{l}_{ub}, \boldsymbol{u}_{ub})$ and $(\boldsymbol{l}_b, \boldsymbol{u}_b)$ are defined as:

$$\begin{cases} \boldsymbol{l}_{ub} = \begin{bmatrix} -a_s Amp\left(\boldsymbol{f}\right) \times \boldsymbol{I}_{n\times 1} \\ -a_s Amp\left(\boldsymbol{f}\right) \times \boldsymbol{I}_{n\times 1} \end{bmatrix} \\ \boldsymbol{u}_{ub} = \begin{bmatrix} a_s Amp\left(\boldsymbol{f}\right) \times \boldsymbol{I}_{n\times 1} \\ a_s Amp\left(\boldsymbol{f}\right) \times \boldsymbol{I}_{n\times 1} \end{bmatrix} \end{cases} \tag{8}$$

$$\begin{cases} \boldsymbol{l}_b = \begin{bmatrix} -a_s Amp\left(\boldsymbol{f}\right) \times \boldsymbol{I}_{(n-2)\times 1} \\ -a_s Amp\left(\boldsymbol{f}\right) \times \boldsymbol{I}_{(n-2)\times 1} \end{bmatrix} \\ \boldsymbol{u}_b = \begin{bmatrix} a_s Amp\left(\boldsymbol{f}\right) \times \boldsymbol{I}_{(n-2)\times 1} \\ a_s Amp\left(\boldsymbol{f}\right) \times \boldsymbol{I}_{(n-2)\times 1} \end{bmatrix} \end{cases} \tag{9}$$

respectively. $\boldsymbol{I}_{n\times 1}$ and $\boldsymbol{I}_{(n-2)\times 1}$ are column vector, of which all the elements are 1. $Amp(\boldsymbol{f})$=$max(\boldsymbol{f})$-$min(\boldsymbol{f})$ denotes the absolute amplitude of $\boldsymbol{f}$. a_s is a scaling factor of the design space. Generally, the design space will expand as a_s increases and increase the computing cost of the optimization. When a_s is set as 10, we found that we could achieve a balance between the computing cost and versatility. A graphic parameter optimization process of i-th handle point is displayed in Fig. 3. By optimizing the position of p_i, the curve near the i-th handle point will move towards the target value. Further optimizing the value of w_i, the radius of the curve near the i-th handle point will be locally adjusted to approximate the target curve. In the actual optimization, all design variables will be optimized simultaneously, achieving a global approximation of the target data.

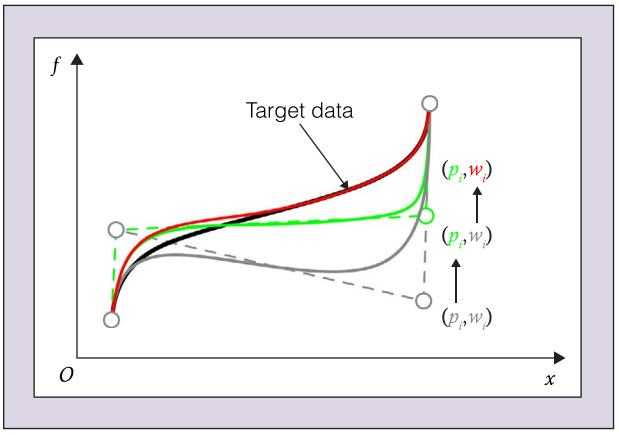

Fig. 3. Schematic diagram of the parameter optimization process.

Sensor Inherent Nonlinearity Calibration

Experimental Setup

Experimental platform of the sensor calibration is depicted in Fig. 4. The calibration object is a micro linear potentiometer with an inherent nonlinearity. The nominal measurement range of the potentiometer is 60 mm. A laser displacement sensor HG-C1200-P is utilized to measure the nonlinear response of the micro linear potentiometer. The nominal measurement range, repeatability and linearity of the laser displacement sensor are 160 mm, 0.2 mm and ±0.2% full scale, respectively. As the probe of the micro linear potentiometer moves within the measurement range, it will produce a displacement response $\boldsymbol{x}$. Meanwhile, the displacement of the probe is measured by the laser displacement sensor as $\boldsymbol{f}$. In the experiment, $\boldsymbol{x}$ and $\boldsymbol{f}$ are sampled by an ADS1115 module, which is a 16-bit Analog-to-Digital Converter (ADC).

Sensor Calibration Results

Fig. 5 illustrates the sensor nonlinearity calibrations by the PCM, UBCM and BCM. The measured $\boldsymbol{x}$, $\boldsymbol{f}$ and the corresponding calibration results are displayed in Fig. 5c. Fig. 5a and Fig.

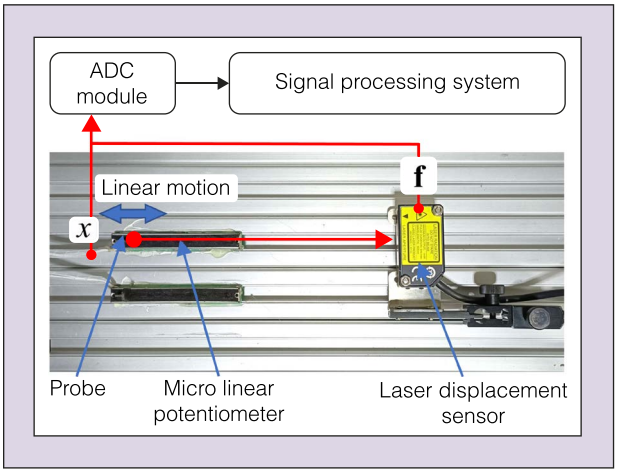

Fig. 4. Linear potentiometer calibration experiments.

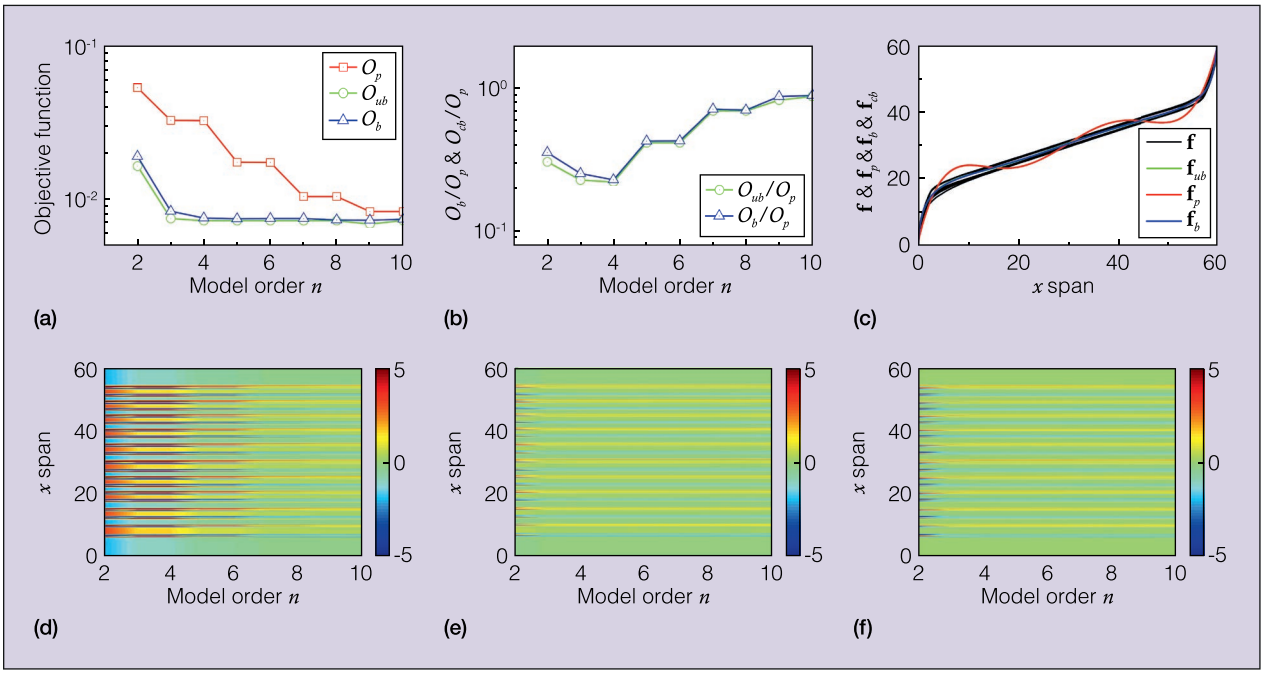

Fig. 5. Sensor nonlinearity calibrations by PCM, UBCM and BCM. (a) and (b) Objective functions comparison. (c) Comparisons of the fifth ordered $\boldsymbol{f}$, $\boldsymbol{f}_p$, $\boldsymbol{f}_{ub}$ and $\boldsymbol{f}_b$. (d)–(f) The distribution of $\boldsymbol{e}_p$, $\boldsymbol{e}_{ub}$ and $\boldsymbol{e}_b$ under different n.

5b display the comparison of O_p, O_{ub}, O_b and O_{ub}/O_p, O_b/O_p under the different model order, respectively. The smaller O_p, O_{ub}, O_b denote the better modeling accuracy. In the present calibrations, the O_{ub}/O_p and O_b/O_p could achieve a minimum of 0.223 and 0.232, respectively. Fig. 5d, Fig. 5e and Fig. 5f display the distribution of $\boldsymbol{e}_p$, $\boldsymbol{e}_{ub}$ and $\boldsymbol{e}_b$ under the different model order n and data span. It reveals that a Runge phenomenon appears in the PCM over the whole measurement range of the linear potentiometer. As a result, the PCM produces a remarkable periodical calibration error over the whole measurement range, as shown in Fig. 5d. Fig. 5c, Fig. 5d and Fig. 5f reveal that the UBCM and BCM models could greatly reduce the measurement error, and that they are smoother than that of the PCM.

Comprehensive Comparison Results and Discussions

In this section, a comprehensive comparison study of the UBCM, BCM and PCM is performed by three typical nonlinear functions, the sine wave, gauss nonlinearity and nonlinear broken line. Although some of the above nonlinearity calibrations are not typical sensor nonlinear characteristic, they are useful in indirect measurement and control applications [23], [24]. Therefore, nonlinearity calibration ability and versatility of a calibration method are of great importance in practical applications.

Sine Wave Nonlinearity Modeling

In temperature sensor denoising applications, the sine wave could be utilized to model the discrete measurement error and then identify the non-linear factors to enhance measurement accuracy [9]. To verify the nonlinear modeling performance of the UBCM, BCM and PCM for sine wave, a standard sine wave f=sin(x), xϵ[0,2π] was tested. The modeling results are compared in Fig. 6. Fig. 6a reveals that O_p, O_{ub},O_b decreases as n increases from 2 to 10. This means that the PCM, UBCM and BCM could improve their calibration accuracy by higher ordered model. In modeling sinusoidal nonlinearity, the UBCM has better calibration accuracy than that of the PCM, since O_{ub}/O_p is smaller than 1. As shown in Fig. 6b, O_{ub}/O_p and O_b/O_p exhibit a decreasing trend first when n is less than 6. As n further increases, O_{ub}/O_p and O_b/O_p appear a rising trend. Generally, the BCM has better calibration efficiency than that of the PCM, for example the 4-8th and 10th ordered calibration model. However, the 2nd, 3rd and 9th ordered BCM has worse calibration efficiency than that of the PCM. The main reason for this phenomenon could be attributed to the boundary constraint properties of the BCM, which could lead to the local distortion of $\boldsymbol{f}_b$.

Gauss Nonlinearity Modeling

In robotic grasping fields, gauss function could be utilized to model the discrete experimental data of the slip resistance of the fingertip for dynamic modeling and analysis [26]. For some robot dynamic control systems, the gauss function could be utilized to describe the dynamic response behavior of the moving parts to accelerate the control speed [25]. To evaluate the nonlinear modeling ability of the UBCM for gauss type nonlinearity, a gauss function $f = ae^{\frac{-(x-b)^2}{2c^2}}$, $x\epsilon$[-10,10] was utilized to evaluate the nonlinearity calibration performance of the PCM, UBCM and BCM. The parameters a, b and c denote the amplitude, central axis and RMS width of the gauss function, respectively. The nonlinear degree of the gauss function could be adjusted by parameter c. Generally, the smaller c denote the stronger local nonlinearity of the gauss function. In this case, the parameters

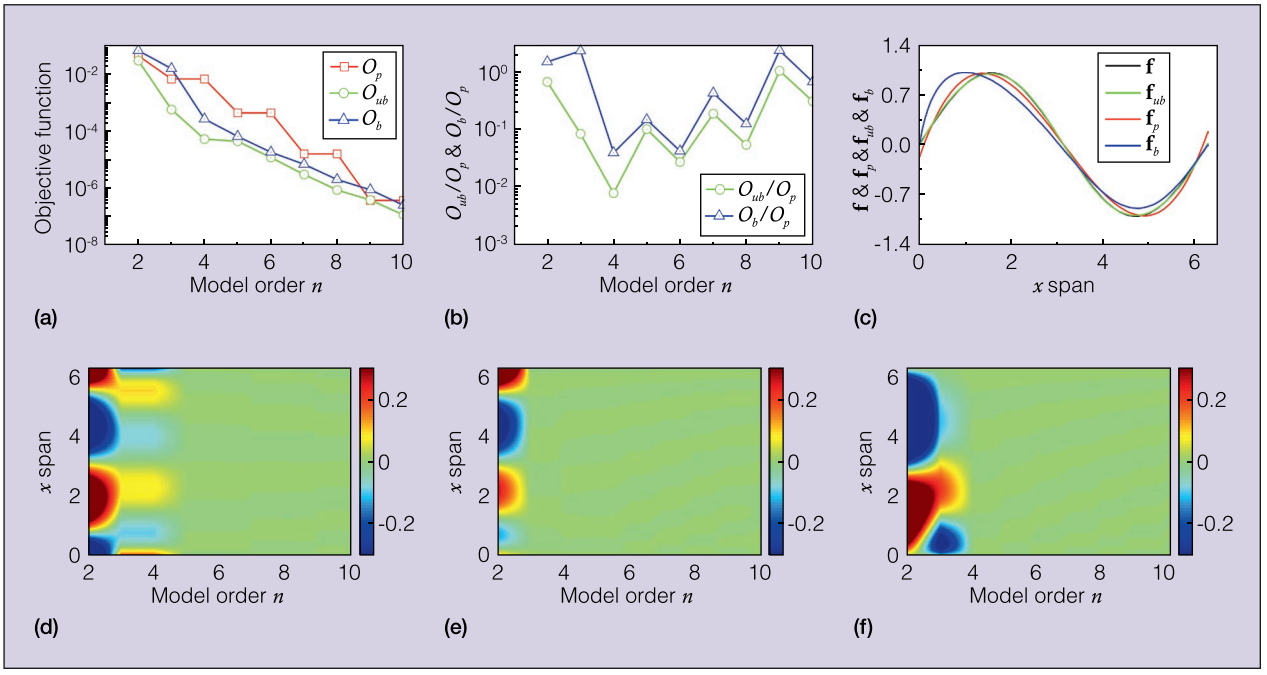

Fig. 6. Sine wave modeling by PCM, UBCM and BCM. (a) and (b) Objective functions comparison. (c) Comparisons of the fifth ordered $\boldsymbol{f}$, $\boldsymbol{f}_p$, and $\boldsymbol{f}_b$. (d)–(f) The distribution of $\boldsymbol{e}_p$, $\boldsymbol{e}_{ub}$ and $\boldsymbol{e}_b$ under different n.

of the gauss function are set as a=1 and b=0, respectively. The nonlinear modeling performance of the UBCM are evaluated under different gauss nonlinearity by adjusting parameter c.

Weak Nonlinearity (c=2): For c=2, the gauss function has a relatively larger RMS width and exhibit a weak nonlinearity, as shown in Fig. 7c. The O_p, O_{ub} and O_b under different n ranging from 2 to 10 are computed and compared in Fig. 7a. It reveals that O_{ub} and O_b decrease faster than that of O_p as n increases. Fig. 7c reveals that f_{ub} and f_b fit well with the f globally. However, f_p still exhibits some obvious calibration error. At the range of about $x\epsilon(-10,-5)$ and $x\epsilon(5,10)$, f_p shows a fluctuation and produces periodical calibration error, which could be observed in Fig. 7c and Fig. 7d. Fig. 7a and Fig. 7b reveal that the UBCM has better calibration accuracy than that of the BCM, since O_{ub} is smaller than O_b. O_{ub}/O_p and O_b/O_p could achieve a minimum of 0.025 and 0.052, respectively.

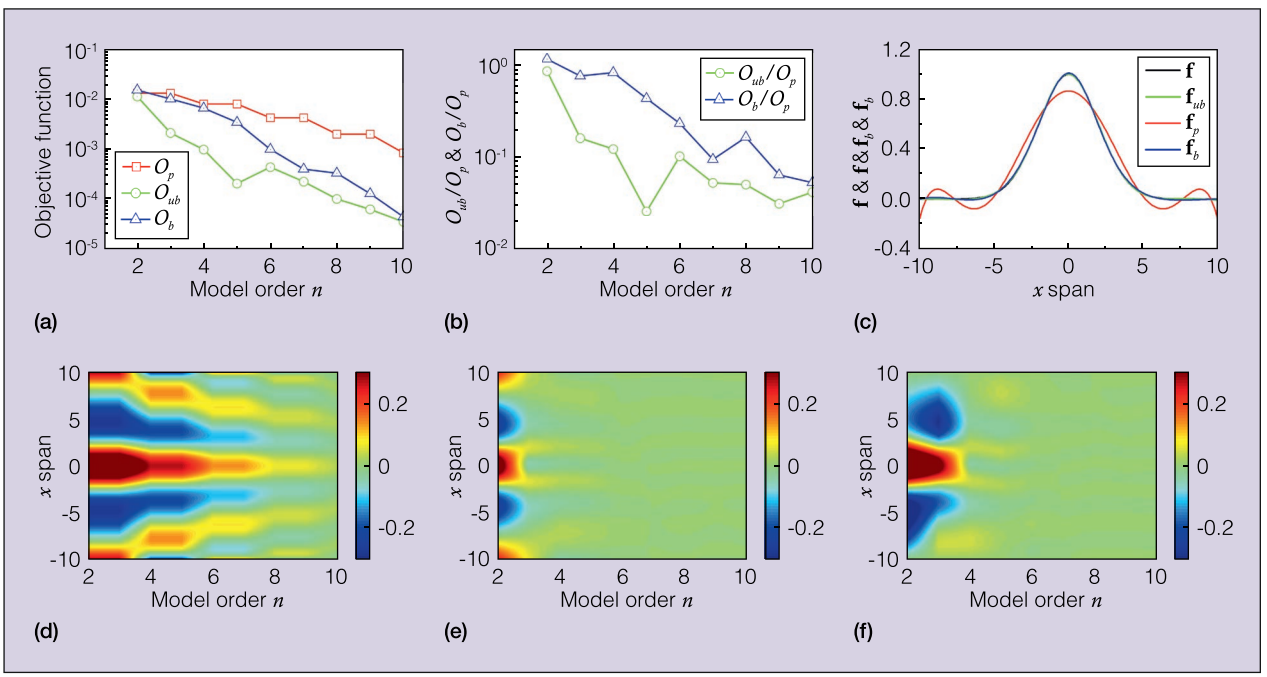

Fig. 7. Gauss nonlinearity modeling by PCM, UBCM and BCM, when a=1, b=0 and c=2. (a) and (b) Objective functions comparison. (c) Comparisons of the fifth ordered $\boldsymbol{f}$, $\boldsymbol{f}_p$, $\boldsymbol{f}_{ub}$ and $\boldsymbol{f}_b$. (d)–(f) The distribution of $\boldsymbol{e}_p$, $\boldsymbol{e}_{ub}$ and $\boldsymbol{e}_b$ under different n.

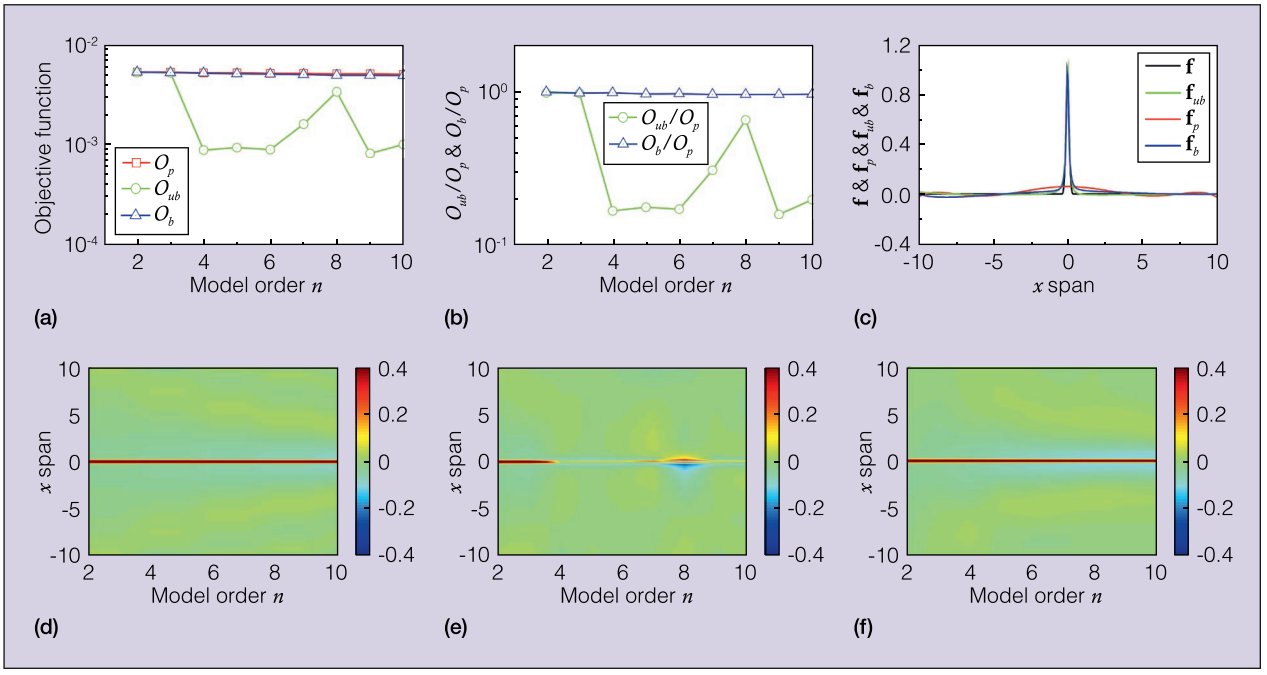

Fig. 8. Gauss nonlinearity modeling by PCM, UBCM and BCM, when a=1, b=0 and c=0.1. (a) and (b) Objective functions comparison. (c) Comparisons of the fifth ordered $\boldsymbol{f}$, $\boldsymbol{f}_p$, $\boldsymbol{f}_{ub}$ and $\boldsymbol{f}_b$. (d)–(f) The distribution of $\boldsymbol{e}_p$, $\boldsymbol{e}_{ub}$ and $\boldsymbol{e}_b$ under different n.

Strong Nonlinearity (c=0.1): To further study the nonlinear modeling ability of PCM, UBCM and BCM, parameter c is reduced to 0.1 to enhance the nonlinearity of the gauss function. As shown in Fig. 8c, the smaller c could lead to a narrower gauss wave. This means the local nonlinearity of the present gauss function will be stronger than that of c=2. Fig. 8a reveals that the O_p and O_b produce little decrement as n increases from 2 to 10. The decrement of the O_{ub} is relatively larger than that of O_p and O_b. This means that for the present gauss nonlinearity, the UBCM could achieve a better calibration accuracy by increasing the model order n. From Fig. 8b, it could be observed that O_{ub}/O_p and O_b/O_p could achieve a minimum of 0.161 and 0.968, respectively.

Comparing Fig. 8d, Fig. 8e, and Fig. 8f, it could be observed that the residual calibration errors mainly occur around x=0. As n increases from 2 to 10, $\boldsymbol{e}_p$ and $\boldsymbol{e}_b$ around x=0 does not show an obvious decreasing trend. This phenomenon could also be observed from Fig. 8c. This indicates that the PCM and BCM are unable to model the local strong nonlinearity of the gauss function. Fig. 8d, Fig. 8e, and Fig. 8f reveal that the UBCM could exhibit an ideal local nonlinearity modeling ability by increasing the model order n.

Modeling of the Nonlinear Broken Line with Inflection Points

In this section, a nonlinear broken line with two inflection points, which is characterized by parameters r and θ, is utilized to evaluate the calibration ability of the PCM, UBCM and BCM, as depicted in Fig. 9. This kind of nonlinearity is quite common in the micro potentiometer as described. Due to the fabrication error, the micro potentiometer often has an inherent saturation nonlinearity. To make a comprehensive evaluation, two parameters, r and θ, respectively, are utilized to adjust the distortion degree and shape of the nonlinear broken line.

Weak Nonlinearity (r=0.25): Generally, the larger r denotes the stronger local nonlinearity of the nonlinear broken line. In this case, r and θ is set as 0.25 and 75°, respectively, to evaluate the calibration performance of PCM, UBCM and BCM. The calibration results of θ=15° are displayed in Fig. 10. From Fig. 10a it could be observed that O_{ub} and O_b are smaller than O_p under different model ordered n. This means that both the UBCM and BCM are optimal calibration approachs for the present nonlinear broken line calibration. Fig. 10b reveals

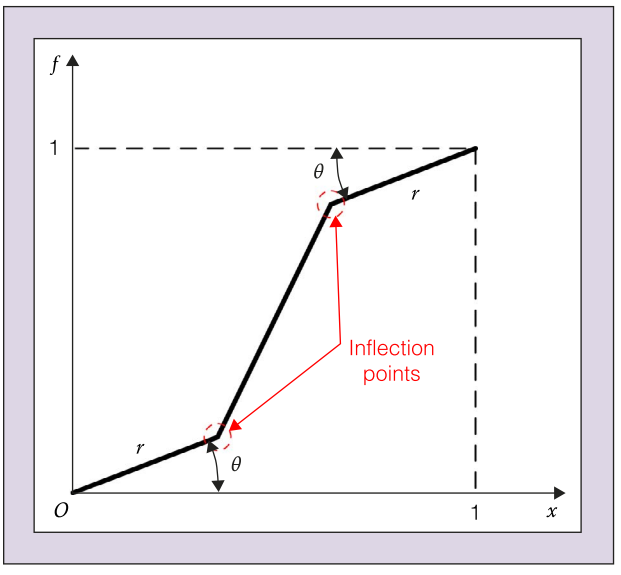

Fig. 9. Illustration of the nonlinear broken line with inflection points.

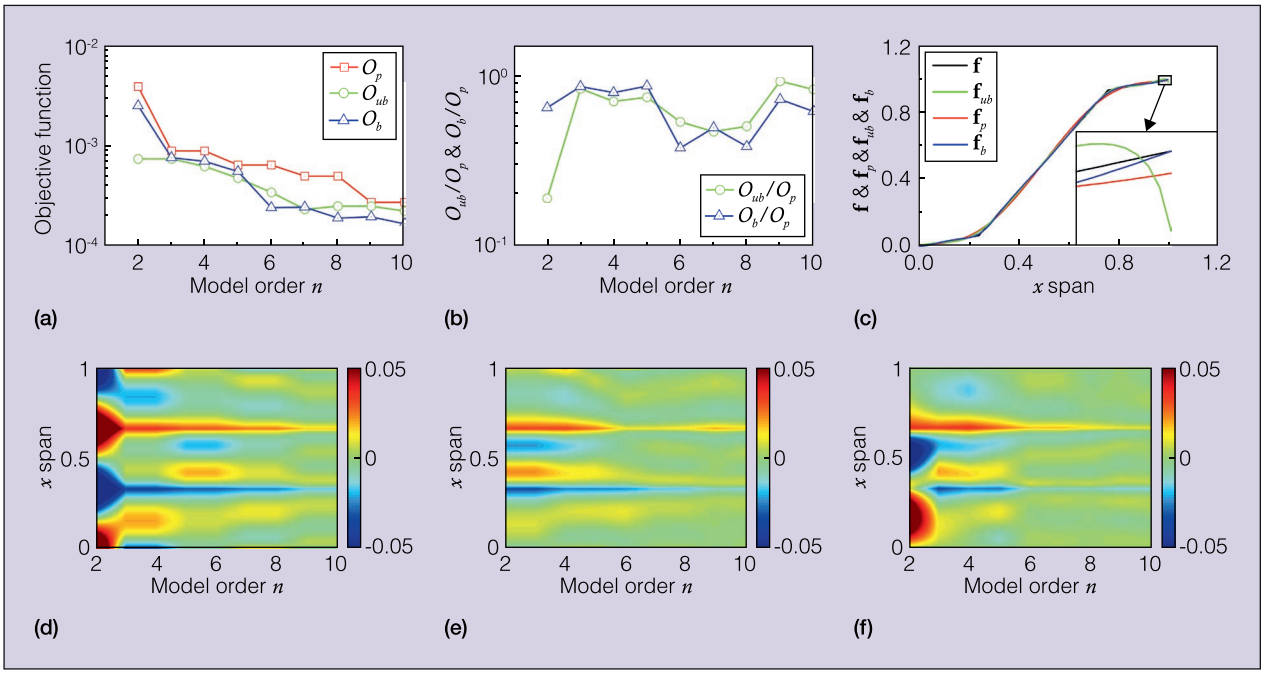

Fig. 10. Nonlinear broken line modeling by PCM, UBCM and BCM, when r=0.25, θ=15°. (a) and (b) Objective functions comparison. (c) Comparisons of the fifth ordered $\mathbf{f}$, $\mathbf{f}_p$, $\mathbf{f}_{ub}$ and $\mathbf{f}_b$. (d)–(f) The distribution of $\mathbf{e}_p$, $\mathbf{e}_{ub}$ and $\mathbf{e}_b$ under different n.

that O_{ub}/O_p and O_b/O_p could achieve a minimum of 0.190 and 0.374, respectively.

Comparing Fig. 10d, Fig. 10e, and Fig. 10f, it could be observed that for the nonlinear broken line, the calibration error mainly occurs at the two inflection points. For the lower-ordered PCM, both the boundary and inflection points will show modeling error. Fig. 10c reveals that f_p produces a sudden decrement around the boundary of x=1. This is a huge drawback of the PCM, since the monotonicity of the PCM could not be guaranteed for the present condition. For a control system, a change of the measurement monotonicity could lead to the unstability of the control process. The same phenomenon could also be observed from Fig. 7c, $x\epsilon$(-10,-5) and $x\epsilon$(5,10).

Strong Nonlinearity (r=0.5): In this case, the parameter r is increased from 0.25 to 0.5 to enhance the nonlinearity of the nonlinear broken line. The corresponding modeling results

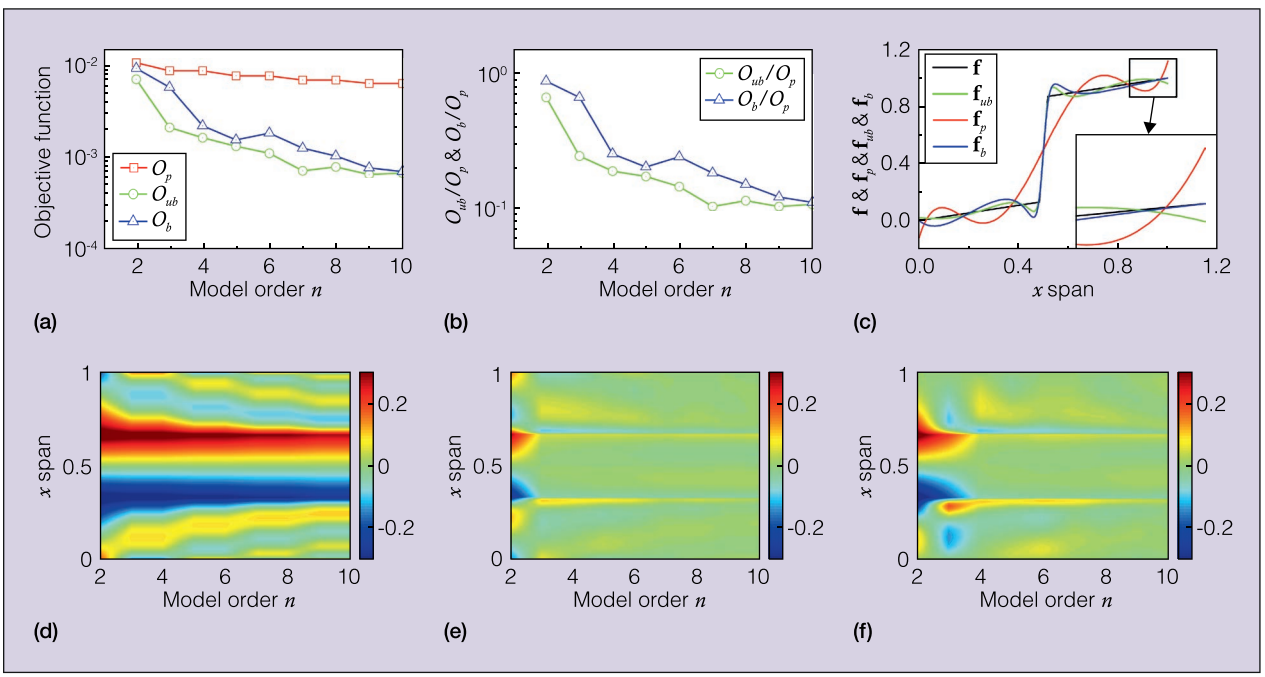

Fig. 11. Nonlinear broken line modeling by PCM, UBCM and BCM, when r=0.5, θ=15°. (a) and (b) Objective functions comparison. (c) Comparisons of the fifth ordered $\mathbf{f}$, $\mathbf{f}_p$, $\mathbf{f}_{ub}$ and $\mathbf{f}_b$. (d)–(f) The distribution of $\mathbf{e}_p$, $\mathbf{e}_{ub}$ and $\mathbf{e}_b$ under different n.

Table 1 – Calibration efficiency comparison of the UBCM, BCM, and PCM under different nonlinear models			
Nonlinear type	**Characteristic parameters**	O_{ub}/O_p	O_b/O_p
Sensor inherent nonlinearity	-	0.2232	0.2318
Sine wave	-	0.0079	0.0401
Gauss wave	a=1, b=0, c=2	0.0254	0.0522
	a=1, b=0, c=0.1	0.1608	0.9676
Nonlinear broken line	r=0.25, 0=15°	0.1899	0.3822
	r=0.5, 0=15°	0.1078	0.1116

are displayed in Fig. 11. As depicted in Fig. 11c, the nonlinear break line will produce a sudden distortion at x=0.5 due to the increment of the parameter r. In this circumstance, the PCM, BCM, and UBCM could not guarantee the monotonicity of the nonlinear broken line. Fig. 11a reveals that when r=0.5, O_{ub} and O_b decrease faster than that of the O_p. As depicted in Fig. 11b, O_{ub}/O_p and O_b/O_p will achieve a minimum of 0.108 and 0.116, respectively. Fig 11d, Fig. 11e, and Fig. 11f reveal that the residual calibration error of the PCM is larger than that of the UBCM and BCM under different model order n.

Modeling Accuracy Comparison

The computed O_{ub}/O_p and O_b/O_p are summarized in Table 1 to make a more intuitive comparison of the calibration accuracy of the PCM, BCM, and UBCM. It reveals that both the minimum of the O_{ub}/O_p and O_b/O_p is smaller than 1. This means that the calibration accuracy of the UBCM and BCM is better than that of the PCM. According to the above comparison study, it could be concluded that the proposed UBCM has better nonlinearity modeling accuracy than that of the previous PCM and BCM.

Conclusions

In this study, an Unconstrained Bezier Calibration Method (UBCM) is presented for the nonlinear system modeling, in which a series of handle points and local weight coefficients are utilized to enhance its nonlinear modeling ability. The proposed UBCM has broad application prospects such as sensor inherent nonlinearity calibration, system modeling and dynamic control. A sensor inherent nonlinearity calibration example is given to exhibit the effectiveness of the proposed UBCM in real applications. Several different nonlinear functions, such as sine wave, gauss nonlinearity and nonlinear broken line, are utilized to test the nonlinear modeling accuracy of the UBCM. A comparison study between the UBCM, BCM and PCM is performed to provide a reference for engineering applications. The conclusions are as follows:

- For the present nonlinearity modeling examples, the PCM, UBCM and BCM could improve their modeling accuracy by increasing its model order n. However, for the gauss nonlinearity and nonlinear broken line, the PCM fluctuates and produces a periodical calibration error that aggravate its modeling accuracy. The UBCM and BCM could suppress the Runge phenomenon and achieve a more accurate calibration than that of the PCM in strong nonlinearity modeling.
- Comparison results reveal that the UBCM has better modeling accuracy than that of the previous PCM and BCM.

Acknowledgment

This research is funded by the National Natural Science Foundation of China (No. 51676099) and various natural science research projects of colleges and universities in Jiangsu Province (No. 20KJB460023).

References

[1] R. Yan, X. Li, Z. Chen, Q. Xu, and X. Chen, "Improving calibration accuracy of a vibration sensor through a closed loop measurement system," *IEEE Instrum. Meas. Mag*., vol. 19, pp. 42–46, 2016.

[2] J. Rohac, M. Sipos, and J. Simanek, "Calibration of low-cost triaxial inertial sensors," *IEEE Instrum. Meas. Mag*., vol. 18, pp. 32–38, 2015.

[3] J. Pieniazek and P. Ciecinski, "Temperature and nonlinearity compensation of pressure sensor with common sensors response," *IEEE Trans. Instrum. Meas*., vol. 69, pp. 1284–1293, 2020.

[4] J. Qi and J. Feng, "Design of robotic soft fingertip for contact sensing," *Measurement*, vol. 147, no. 106812, 2019.

[5] Z. Guo, C. Lu, Y. Wang, D. Liu, M. Huang, and X. Li, "Design and experimental research of a temperature compensation system for silicon-on-sapphire pressure sensors," *IEEE Sensors J*., vol. 17, pp. 709–715, 2016.

[6] V. N. Kumar and K.V. L. Narayana, "Development of an ANN-based pressure transducer," *IEEE Sensors J*., vol. 16, pp. 53–60, 2015.

[7] J. Pieniążek and P. Cieciński, "Measurement device with learned sensor," in *Proc. 2014 IEEE Metrology for Aerospace (MetroAeroSpace)*, pp. 260–264, 2014.

[8] A. Nugroho, A. B. Gumelar, E. M. Yuniarno, and M. H. Purnomo, "Accelerometer calibration method based on polynomial curve fitting," in *Proc. 2020 Int. Sem. App. Technol. Information and Communi. (iSemantic)*, pp. 592–596, 2020.

[9] Y. Zhang, R. Wang, S. Li, and S. Qi, "Temperature sensor denoising algorithm based on curve fitting and compound kalman filtering," *Sensors*, vol. 20, no. 1959, 2020.

[10] J. Wu, Y. Su, Y. Cheng, X. Shao, C. Deng, and C. Liu, "Multi-sensor information fusion for remaining useful life prediction

of machining tools by adaptive network based fuzzy inference system," *Applied Soft Computing*, vol. 68, pp. 13–23, 2018.

[11] M. R. Safaei, A. Hajizadeh, M. Afrand, C. Qi, H. Yarmand, and N.W.B.M. Zulkifli, "Evaluating the effect of temperature and concentration on the thermal conductivity of ZnO-TiO2/EG hybrid nanofluid using artificial neural network and curve fitting on experimental data," *Physica A: Statistical Mechanics Appl.*, vol. 519, 2019.

[12] A.A.A.A. Alrashed, A. Karimipour, S.A. Bagherzadeh, M.R. Safaei, and M. Afrand, "Electro- and thermophysical properties of water-based nanofluids containing copper ferrite nanoparticles coated with silica:experimental data, modeling through enhanced ANN and curve fitting," *Int. J. Heat and Mass Transfer*, vol. 127, pp. 925–935, 2018.

[13] H. Wu, A.A.A.A. Alrashed, A. A. Barzinjy, A. Shahsavar, A. Karimi, and P. Talebizadehsardari, "Curve-fitting on experimental thermal conductivity of motor oil under influence of hybrid nano additives containing multi-walled carbon nanotubes and zinc oxide," *Physica A: Statistical Mechanics Appl.*, vol. 535, 2019.

[14] C. Li, F. Cordovilla, R. Jagdheesh, and J. L. Ocaña, "Design optimization and fabrication of a novel structural SOI piezoresistive pressure sensor with high accuracy," *Sensors*, vol. 18, 2018.

[15] A.V. Tran, X. Zhang, and B. Zhu, "Mechanical structural design of a piezoresistive pressure sensor for low-pressure measurement: a computational analysis by increases in the sensor sensitivity, *Sensors*, vol. 18, 2018.

[16] Y. Chen, "High-order polynomial interpolation based on the interpolation center's neighborhood, the amendment to the Runge phenomenon," in *Proc. 2009 WRI World Congress on Software Engineering*, pp. 345–348, 2009.

[17] B. Fornberg and J. Zuev, "The Runge phenomenon and spatially variable shape parameters in RBF interpolation," *Computers and Mathematics with Appl.*, vol. 54, pp. 379–398, 2007.

[18] C. Ye, S. Feng, Z. Xue, C. Guo, and Y. Zhang, "Defeating Runge problem by coefficients and order determination method with various approximation polynomials," in *Proc. 37th Chinese Control Conf. (CCC)*, 2018, pp. 8622–8627, 2018.

[19] B. Yan, "Research on linearity continuous correction technology of carbon film potentiometer linearity," Harbin Institute of Technology Master degree thesis, Harbin, China, 2019.

[20] H. Hua, Z. Liao, X. Wu, and Y. Chen, "A Bezier based state calibrating method for low-cost potentiometer with inherent nonlinearity," *Measurement*, vol. 178, no. 109325, 2021.

[21] J. P . Boyd and J. R. Ong, "Exponentially-convergent strategies for defeating the Runge phenomenon for the approximation of non-periodic functions, part two: multi-interval polynomial schemes and multidomain Chebyshev interpolation," *Applied Numerical Mathematics*, vol. 61, pp. 460-472, 2011.

[22] P. N. Sergi, N. De la Oliva, J. del Valle, X. Navarro, and S. Micera, "Physically consistent scar tissue dynamics from scattered set of data: a novel computational approach to avoid the onset of the Runge phenomenon," *Applied Sciences*, vol. 11, no. 8568, 2021.

[23] H. Hua, Z. Liao, X. W. Wu, Y. Chen, and C. Feng, "A back-drivable linear force actuator for adaptive grasping," *J. Mech. Sci. Technol.*, vol. 36, no. 8, pp. 4213-4220, 2022.

[24] H. Hua and Z. Liao, "Design, analysis and experiment of an underactuated robotic gripper actuated by linear series elastic actuator," *J. Mechanisms and Robotics*, vol. 15, no. 2, Apr. 2023.

[25] K. Tanaka, S. Nishikawa, R. Niiyama, and Y. Kuniyoshi, "Immediate generation of jump-and-hit motions by a pneumatic humanoid robot using a lookup table of learned dynamics," *IEEE Robotics Automation Letters*, vol. 6, pp. 5557–5564, 2021.

[26] D. Cardin-Catalan, S. Ceppetelli, A. P. del Pobil, and A. Morales, "Design and analysis of a variable-stiffness robotic gripper," *Alexandria Eng. J.*, vol. 61, pp. 1235–1248, 2022.

Hongliang Hua (huahl123@126.com) is an Assistant Professor at Changzhou Institute of Technology in Changzhou, China. His current research interests include robotic grasping control and structural optimization. He received the Ph.D. degree in mechanical engineering from Nanjing University of Science and Technology in Nanjing, China.

Jingbo Zhao is a Professor at Changzhou Institute of Technology in Changzhou, China. His current research interests include measurement and control. He received the Ph.D. degree in vehicle engineering from Jiangsu University in Zhenjiang, China.

Zhenqiang Liao is a Professor at Nanjing University of Science and Technology in Nanjing, China. His current research interests include robotics and control. He received the Ph.D. degree in mechanical engineering from Nanjing University of Science and Technology in Nanjing, China.

Yongjiang Chen is a Professor at Changzhou Institute of Technology in Changzhou, China. His current research interests include measurement and control. He received the Ph.D. degree in mechanical engineering from Southeast University in Nanjing, China.